Chiral topological light for detecting robust enantio-sensitive observables

N. Mayer[1], D. Ayuso[2], M. Ivanov[1,2,3], E. Pisanty[4], O. Smirnova [1,5]

[1] Max-Born-Institute, Max-Born str. 2A, 12489 Berlin, Germany
[2] Department of Physics, Humboldt University, Newtonstr. 15, D-12489 Berlin, Germany
[3] Blackett Laboratory, Imperial College London, SW7 2AZ London, United Kingdom.
[4] Department of Physics, Technical University Berlin, Berlin, Germany

Topological response of matter to electromagnetic fields is the property in demand in materials design [1] and metrology [2] due to its robustness against the noise or decoherence, stimulating recent advances in ultrafast photonics. [3, 4]. Similar topological robustness is desirable in enantio-sensitive detection but is currently missing. We introduce the concept of a chiral topological light - a hybrid between the vortex beam and synthetic chiral light, which interacts with chiral molecules extremely efficiently due to the electric dipole nature of this interaction. An integer topological charge is encoded in the azymuthal evolution of light's handedness. The topological protection arises due to mapping of topological charge into the intensity of the far-field profile of non-linear optical response, where enantio-sensitivity arises as its spatial rotation. The intensity maxima are robust against noise and enable detection of percent level enantiomeric excesses in mixtures as we demonstrate numerically for randomly oriented fenchone molecules. Next we show that using the topological charge as a parameter one can reconstruct the chiral and achiral components of non-linear response. Our work opens a way to the new extremely efficient and robust chiroptical spectroscopies with attosecond time resolution.

Topological properties of electronic response to electromagnetic fields in solid state systems as well as in photonic structures are being actively harvested to obtain robust observables, such as e.g. edge currents protected with respect to material imperfections in topological insulators [5] or topologically protected light propagation pathways in their photonic analogs [6]. Similar robustness of enantio-sensitive optical signals in chiral molecular gases or liquids is much desired for analytical purposes, but is currently missing. While the first ideas connecting topological and chiral properties of electronic response[7, 8] or microwave signals in molecular gases[9, 10] are starting to emerge, similar ideas can not be mapped to optical response. Topologically non-trivial optical signals can be achieved due to vortex beams – beams carrying orbital angular momentum (OAM) – and characterised by an integer topological charge representing the number of spiral revolutions of light's wavefront in space within one wavelength [11]. Vortex light has been successfully used for chiral detection in the hard X-ray region [12, 13], however its natural enantio-sensitivity in optical domain is weak: vortex light is not enantio-sensitive in the electric dipole regime. Here we introduce the chiral topological light which takes advantage of the global topological structure of vortex light and high enantio-sensitivity of synthetic chiral light, for obtaining topologically robust and highly enantio-sensitive ultrafast optical response.

Synthetic chiral light [14] encodes chirality in the temporal evolution of its three dimensional polarization vector: the Lissajous figure drawn by the tip of the electric field during one cycle of evolution is chiral. Its high enantio-sensitivity is due to local, i.e. electric dipole, nature of induced chiral response. The handedness of light can be controlled by the phase delay between its several (at least two) frequency components both locally in

every point in space and globally in the interaction region, offering a unique opportunity to ignite structured in space chiral emitters with controlled handedness in initially amorphous chiral medium, such as molecular gas [15, 16]. Here we show that this opportunity can be used to create topologically robust enantio-sensitive observables.

Our key idea is to imprint the topological parameter of the vortex beam, its topological charge C, on the azimuthal phase of the chiral correlation function h characterising the handedness of the synthetic chiral light: $\arg h(\theta) = C\theta + \phi_L$, where θ is azimuthal angle, ϕ_L is the enantio-sensitive phase of synthetic chiral light. We show that the intensity of emission triggered by such light depends on both chiral and topological phases of h as well as the enantio-sensitive phase ϕ_M introduced by molecular medium: $I(\theta) \propto \cos(\phi_M - \phi_L + C\theta)$. Using numerical simulations we demonstrate that azimuthal intensity profile is modulated in a topologically robust and molecular specific way leading to large enantio-sensitive offset between intensity maxima (or minima) in opposite enantiomers $\Delta\theta = \pi/C$. What's more, the topologically controlled angular off-set persists for small amounts of enantiomeric excess and can be detected even in dilute mixtures.

To demonstrate these ideas we now focus on specific realization of chiral topological light which involves Laguerre-Gaussian beams with bicircular counter-rotating polarization propagating along the z-axis with frequencies ω and 2ω and orbital angular momentum ℓ_ω and $\ell_{2\omega}$. At the focus of the beams $z = 0$, the Cartesian components of the fields in the orthogonal plane (x, y)

are:

$$\mathbf{E}^{\perp}_{\pm,r\omega} = \mathcal{E}_{r\omega} e^{-\frac{\rho^2}{W_0^2}} \left(\frac{\sqrt{2}\rho}{W_0}\right)^{|\ell_{r\omega}|} e^{\mathrm{i}\ell_{r\omega}\theta} e^{\mathrm{i}\phi_{r\omega}}$$

$$\frac{(\mathbf{e}_x - \mathrm{i}m_{r\omega}\mathbf{e}_y)}{\sqrt{2}} \tag{1}$$

where $\mathcal{E}_{r\omega} = \sqrt{I_{r\omega}}$ is the field strength, W_0 is the beam waist, $\phi_{r\omega}$ is the CEP phase, $\rho = \sqrt{x^2 + y^2}$, $\theta = \arctan(y/x)$ are the polar and azimuthal coordinates and $m_{r\omega}$ indicates right ($m_{r\omega} = 1$) or left ($m_{r\omega} = -1$) circular polarization. Near the focus this field develops a longitudinal component along the z-axis $E_z = -(\mathrm{i}/k)\nabla_{\perp} \cdot \mathbf{E}_{\perp}$ (see Fig. 1a):

$$\mathbf{E}^{z}_{\pm,r\omega} = -\frac{\mathrm{i}\mathcal{E}_{r\omega}}{\sqrt{2}k_{r\omega}} e^{-\frac{\rho^2}{W_0^2}} \left(\frac{\sqrt{2}}{W_0}\right)^{|\ell_{r\omega}|} \rho^{|\ell_{r\omega}|-1} \tag{2}$$

$$e^{\mathrm{i}(l_{r\omega}+m_{r\omega})\theta} \left(|\ell_{r\omega}| - m_{r\omega}\ell_{r\omega} - \frac{2\rho^2}{W_0^2}\right)\mathbf{e}_z$$

taking the light polarization vector out of polarization plane (x,y) - a prerequisite for creating synthetic chiral light. Indeed, the total bichromatic electric field $\mathbf{E}(x,y) = \mathbf{E}_{\pm,\omega} + \mathbf{E}_{\pm,2\omega}$, combining the longitudinal and transverse field components for each color $\mathbf{E}_{\pm,r\omega} = \mathbf{E}^{\perp}_{\pm,r\omega} + \mathbf{E}^{z}_{\pm,r\omega}$ ($r = 1,2$, is an example of a synthetic chiral light [14].

The chiral Lissajous figure drawn by the polarization vector of such light over a laser cycle is chiral (see inset in Fig. 1a) and its handedness is controlled by the relative phase between the two colors $\phi_{2\omega,\omega} = 2\phi_\omega - \phi_{2\omega}$ [14], which in turn depends on radial and azimuthal coordinates forming a chiral vortex with the topological charge (see Methods):

$$C = \ell_{2\omega} - 2\ell_\omega + m_{2\omega} - 2m_\omega. \tag{3}$$

Indeed, the Lissajous curve drawn by the polarization vector of the electric field over one laser cycle changes with the azimuthal angle, switching handedness $2C$ times as the azimuthal angle changes by one period (Fig. 1b). Hence, the superposition of two tightly-focused OAM beams at commensurate frequencies gives rise to a chiral vortex, i.e. a vortex beam displaying chirality locally at each given point with an azimuthally varying handedness characterized by an integer topological charge C.

Figure 1c visualises the chiral vortex by displaying the beam total intensity $|\mathbf{E}(x,y)|^2$, the absolute value $|h^{(5)}(x,y)|$ and the phase $\arg[h^{(5)}(x,y)|$ of the chiral correlation function for OAM $(\ell_\omega, \ell_{2\omega}) = (1,-1)$ and SAM $m_\omega = -m_{2\omega} = 1$. Both the chirality and the total intensity maximize along rings (see Figure 1c), typical for vortex beams, while the topological charge $C = -6$ characterizes the azimuthal phase distribution of the light's handedness quantified by the chiral correlation function.

The chiral topological charge C is highly tunable thanks to its dependence on the OAM of the two beams,

which can take any integer value from $-\infty$ to ∞, enabling chiral vortices with arbitrarily high chiral topological charge. OAM- controlled synthetic chiral light offers additional benefit: by balancing orbital angular momenta of the two beams such that $C = 0$, one can create globally chiral light with a well-defined handedness bypassing the somewhat limiting requirement of non-collinear beam geometry [14]. Fig. 2b shows the near-field intensity of harmonic 18 for randomly oriented (+)Fenchone and (-)Fenchone driven by the chiral topological light with fundamental frequency $\omega = 0.044$ a.u. (1033 nm), peak intensity $I_0 = E_0^2 = 5 \cdot 10^{14}$ W/cm^2 and a beam waist of $W_0 = 2.5$ μm at the jet position $z = 0$, simulated using our DFT-based S-matrix approach (see Methods and Refs.[15, 17]). The peaks in azimuthal direction are due to the constructive interference between chiral and achiral emission channels which occurs at the angles $\theta = [2\pi n + (\phi_L - \phi_M)]/C$; the angular position of the peaks is therefore enantio-sensitive, as swapping molecular enantiomer corresponds to π shift of the molecular phase $\phi_M \rightarrow \phi_M + \pi$. The number of peaks is controlled by the topological charge $C = -6$ and is a topologically protected quantity.

The far field signal offers additional unique benefits due to spatial filtering of chiral and achiral signals. The opportunity to efficiently separate chiral and achiral signal in space arises due to different selection rules for chiral and achiral quantum pathways, which in chiral topological light translates into different orbital angular momentum content of respective signals (Methods). The chiral signal has low orbital angular momentum content, while the achiral signal has high orbital momentum content: the difference between the two is controlled by the topological charge and can be large as e.g. in our case. As a result, chiral signal with low orbital angular momentum content (OAM=1,-1) is only weakly divergent and appears in the center of the far field image (Fig. 2b), while highly divergent due to high orbital momentum content (OAM=5,-5) achiral signal resides in the outer ring (Fig. 2b). Thus, in a racemic or achiral medium the inner signal will not be present (Fig. 3b) offering topologically robust approach to detecting chirality in mixtures with low enantiomeric excess, which we demonstrate below. Robust detection of small enantiomeric excess in chiral mixtures relies on the fact that the far-field images for racemic and non-racemic mixtures have topologically distinct shapes. The racemic signal is structureless in the inner ring, but even small enantiomeric excess triggers the $|C|$-fold symmetry of the intensity distribution (see, 3a,c, where $|C| = 6$, for enantiomeric excess $\pm 4\%$). Topological transition in the enantiosensitive signal as a function of enantiomeric excess and azimuthal angle in the far-field is illustrated in Figs. 3d,e. Fig. 3d shows the radially integrated signal of the inner ring, while Fig. 3e shows the radially integrated signal of the outer ring. Both signals show periodic oscillations as a function of azimuthal angle, with minima (maxima) occuring $|C| = 6$ times. The maxima (minima) of signal intensity versus
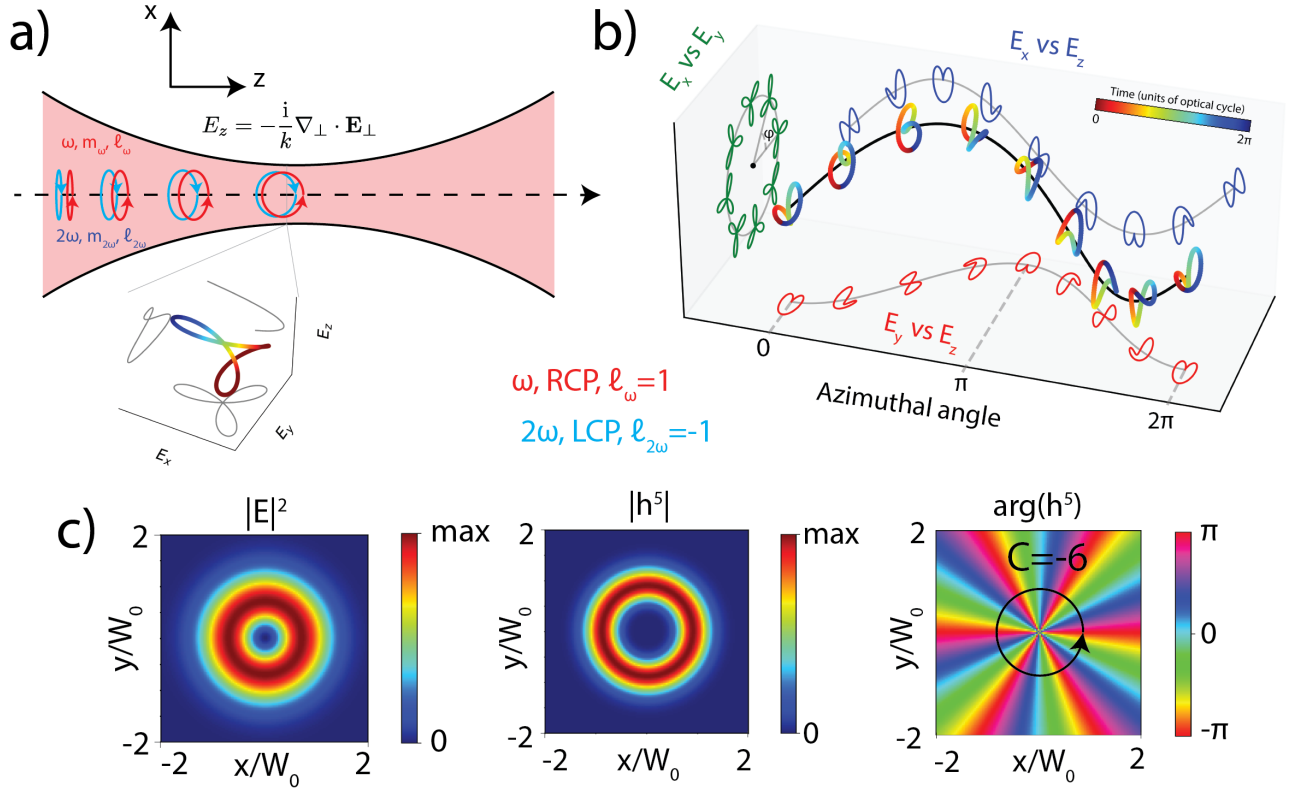
FIG. 1. The concept of chiral vortex light for bicircular counter-rotating $m_\omega = -m_{2\omega} = 1$ beams carrying OAMs $\ell_\omega = -\ell_{2\omega} = 1$. **a)** Tight-focusing of bicircular counter-rotating Gaussian beams induces a longitudinal field, resulting in a synthetic chiral field whose polarization vector draws a chiral Lissajous over one laser cycle. **b)** Evolution of the chiral Lissajous curves with respect to the azimuthal angle $\phi = \arctan(y/x)$ at a given radial position $\rho = \sqrt{x^2 + y^2}$ at $z = 0$ for a chiral vortex with $\ell_\omega = -\ell_{2\omega} = 1$. **c)** Slices through the electric field distribution at $z = 0$. The figures show the total intensity of the electric field $|\mathbf{E}|^2$, the absolute value of the chiral correlation function $|h^{(5)}|$ and its phase distribution $\arg\left[h^{(5)}\right]$. The phase distribution of $h^{(5)}$ describes the spatial distribution of the handedness of light and is characterized by a topological charge $C = -6$. The x and y coordinates are scaled to the width W_0 of the beams at the focus.

azimuthal angle are shifted by $2\pi/|C| = 30^o$ for positive and negative enantiomeric excess. Thus, both in inner and outer rings at $ee = 0$ we observe a jump in signal intensity signifying a topological transition. These topological transitions can be easily detected e.g. by performing a Fourier analysis of the signal with respect to the azimuthal angle as a function of enantiomeric excess. The solid red lines in Fig. 3f show the phase of Fourier component f_6 oscillating at the $C = 6$ frequency of the outer (top plot) and inner (bottom plot) signals as a function of the enantiomeric excess. A clear π phase jump is observed at $ee = 0\%$, indicating the switch in the handedness of the mixture.

To verify the topological robustness of our signal we have included noise in our simulations (see the Methods section) via intensity fluctuations of the driving fields. The blue solid lines Fig. 3f show the phase of the Fourier component f_6 when noise is included. It is clear that the π jump of the phase is robust against noise, as it is topologically protected by the properties of our chiral topological light.

Chiral topological light also offers an exciting opportunity to reconstruct the phases and amplitudes of both chiral and achiral pathways contributing to a given harmonic order in a topologically robust way. Such reconstruction enables complete characterization of underlying chiral electron or vibrational dynamics on attosecond to femtosecond timescales – the holy grail of attosecond molecular spectroscopy. Indeed, the far-field signal for a mixture of right-handed and left-handed molecules is given by

$$S_{ee}(\Omega, \mathbf{k}) = |A_{ach}(\Omega, \mathbf{k}) + ee A_{ch}(\Omega, \mathbf{k})|^2 = \\ |A_{ach}|^2 + ee^2 |A_{ch}|^2 + \\ ee\left(A_{ach}^* A_{ch} + A_{ach} A_{ch}^*\right) \quad (4)$$

First we reconstruct the amplitudes of chiral and achiral components and then we reconstruct the relative phases between them. The amplitude $|A_{ch}|$ of the chiral component can be found via $|A_{ch}|^2 = (S_{ee=1} + S_{ee=-1})/2 - S_{ee=0}$.
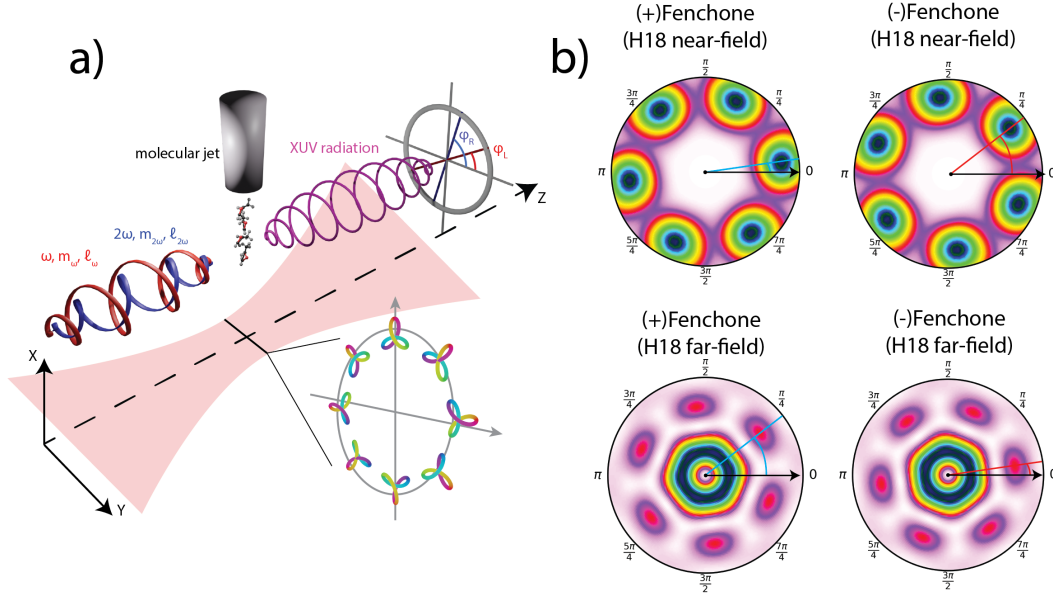
FIG. 2. Enantio-sensitive High-Harmonic spectroscopy using chiral vortices. **a)** Schematic depiction of the experimental setup. Two counter-rotating circularly polarized beams with frequencies ω and 2ω carrying OAM ℓ_ω and $\ell_{2\omega}$ are tightly-focused on a thin gas jet of chiral molecules. The resulting synthetic chiral field posses an azimuthally evolving handedness (inset); the resulting XUV radiation emitted through the HHG process is detected in the far-field. Chiral discrimination can be accomplished by measuring the offset angles of the azimuthal interference patterns in the spatial profile of the high harmonics. **b)** Near-field (top row) and far-field (bottom row) spatial profiles of H18 in (+)Fenchone (left column) or (-)Fenchone (right column), displaying the enantio-sensitive rotation of the harmonic profiles.

The amplitude $|A_{ach}|$ of the achiral component can be extracted from the racemic mixture signal $|A_{ach}|^2 = S_{ee=0}$.

The analysis of multiphoton pathways (see Methods) shows that while the chiral component of emission is dominated by a single pathway, two pathways, one of which is stronger than the other, contribute to the achiral component. For example for a final SAM co-rotating with the 2ω field, one achiral pathway (the dominant one) includes the absorption of a circularly polarized photon 2ω together with a longitudinally polarized 2ω photon and emission of a longitudinally polarized ω photon. The second achiral pathway involves the absorption of 4ω longitudinally polarized photons and the emission of a circularly polarized ω photon. For the OAM and SAM of the driving fields considered here ($\ell_\omega = m_\omega = 1$, $\ell_{2\omega} = m_{2\omega} = -1$) one achiral pathway has final OAM $\ell_{ach,1} = \ell_{ch} + C$ and the other one has final OAM $\ell_{ach,2} = \ell_{ch} - C$; thus $\ell_{ach,1} - \ell_{ach,2} = 2C$. Thus, the relative phase between these two achiral pathways oscillates as $2(C\psi + \phi_L)$, where C is the topological charge, ψ is the far-field angle and $\phi_L = 2\phi_\omega - \phi_{2\omega}$ is the laser field phase, yielding the overall achiral signal:

$$|A_{ach}|^2 = |A_{ach,1}|^2 + |A_{ach,2}|^2 +$$
$$2\sqrt{|A_{ach,1}||A_{ach,2}|}\cos\left(2(C\psi + \phi_L) + \phi_{ach}\right) \quad (5)$$

Here $\phi_{ach} = \phi_{ach,1} - \phi_{ach,2}$ is the (molecular-specific) relative phase between the two achiral pathways. In order

to find this phase, we set the phase of the laser field to $\phi_L = 0$ and fit the signal of the outer ring (see Fig. 3b) with respect of the azimuthal angle to the fit function (see SI) $f_{fit}(\psi) \propto \cos\left(2C\psi + \phi_{ach}\right)$.
Armed with the knowledge of $|A_{ach}|^2$, $|A_{ch}|^2$ and ϕ_{ach}, we can now reconstruct the phase of the chiral component ϕ_{ch} from the total signal:

$$S_{ee}(\Omega,\mathbf{k}) = |A_{ach}(\Omega,\mathbf{k}) + ee A_{ch}(\Omega,\mathbf{k})|^2 =$$
$$|A_{ach}|^2 + ee^2|A_{ch}|^2 + ee\left(A_{ach}^* A_{ch} + A_{ach} A_{ch}^*\right)$$
$$= |A_{ach,1}|^2 + |A_{ach,2}|^2 + |A_{ch}|^2 +$$
$$2\sqrt{|A_{ach,1}||A_{ach,2}|}\cos(2C\psi + \phi_{ach}) + \quad (6)$$
$$2ee\sqrt{|A_{ach,1}||A_{ch}|}\cos(C\psi + \phi_{ch}) +$$
$$2ee\sqrt{|A_{ach,2}||A_{ch}|}\cos(-C\psi + \phi_{ch} + \phi_{ach})$$

To reconstruct ϕ_{ch}, we first rewrite the achiral magnitudes as $|A_{ach,2}|^2 = \lambda|A_{ach,1}|^2$, where $\lambda \geq 0$ corresponds to the ratio between the strength of the two pathways. Next, we minimize the difference between the numerically-found signal and the fit function (Eq. 6) taking the strength of the achiral pathway $|A_{ach,1}|^2$, the ratio λ and the phase ϕ_{ch} as free parameters. Successful fitting requires good initial guess for the free parameters. The initial guess for the the strength of the achiral component is $S_{ee=0}/2$, the ratio of two achiral channels can be easily estimated from the ratio of longitudinal and
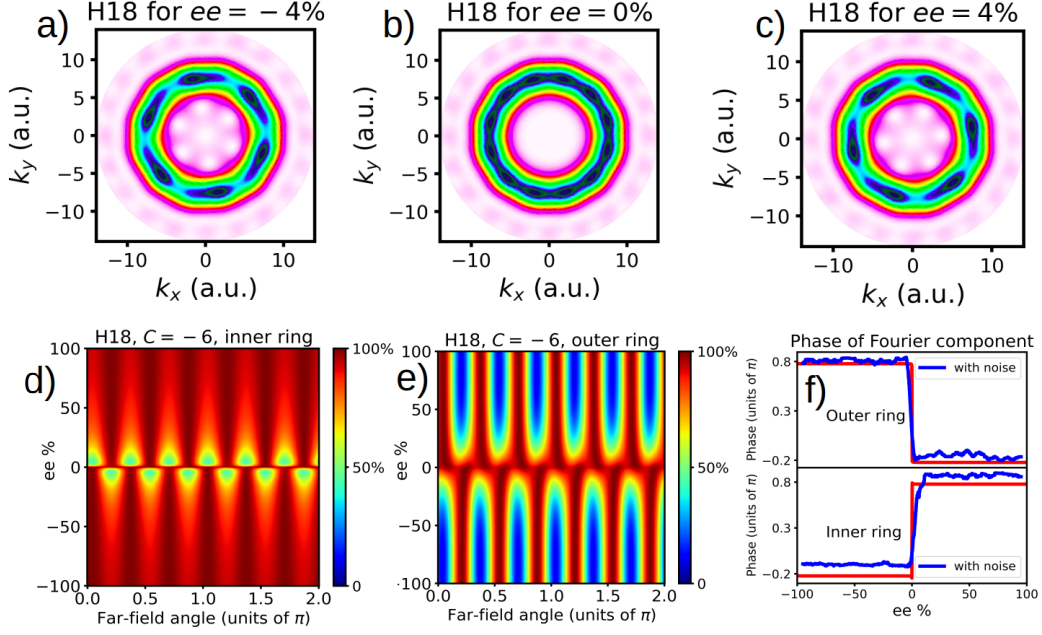
FIG. 3. Chiral discrimination using chiral vortices. **a,b,c)** Far-field profiles of H18 for a mixture of right-handed and left-handed molecules with enantiomeric excess $ee = C_R - C_L$ of -4%, 0 and 4% (**a**, **b** and **c** respectively), where C_R and C_L are the concentration of the right- and left-handed molecules. **d)** Radially integrated around the inner ring, angle-resolved far-field H18 signal as a function of the enantiomeric excess for a chiral vortex with $C = -6$. For each enantiomeric excess we normalize the profile to its maximum for better visibility. **e)** Radially integrated around the outer ring, angle-resolved far-field H18 signal as a function of the enantiomeric excess for a chiral vortex with $C = -6$. For each enantiomeric excess we normalize the profile to its maximum for better visibility. **f)** Phase of the Fourier component f_6 of the inner and outer ring as a function of enantiomeric excess for simulations excluding (solid red line) and including (solid blue line) noise.

transversal light components, yielding $\lambda = 0.01$. As we have no prior knowledge on ϕ_{ch}, we repeated the procedure for different initial guesses looking to obtain the best result.

Fig. 4 shows the results of the reconstruction for H18 and the SAM component $m = 1$ (the results for SAM $m = -1$ are shown in the Supplementary Material). Figs. 4a,b show respectively the reconstructed and numerically obtained far-field profile for H18, while the top right figure shows the difference between the two maps normalized by $\int |f_{rec}(\mathbf{k}) + f_{target}(\mathbf{k})|d\mathbf{k}$. The reconstructed images are in excellent agreement, with errors is on the order of 10^{-5}, i.e. 0.01 %. The reconstructed phase of the far-field dipole moment ($d = d_{ach} + d_{ch}$) is shown in Fig. 4d, while Fig. 4e shows the phase of the chiral component and Fig. 4f the relative phase between the achiral components. As shown in the Supplementary Material, the main differences between the reconstructed and numerically obtained images are noticeable either on the outer edge of the spatial profile (where the signal intensity is very weak) or near the center of the vortex at $\mathbf{r} = 0$, where its phase is not well defined. Note that we allow ourselves to change a global overall phase ϕ_0 in order to match the reconstructed and numerical dipole moment such that $d_{rec} = d_{num}e^{i\phi_0}$.

We note that the uniqueness of the solution given by

the reconstruction algorithm relies on the analysis of the involved pathways. The hierarchy of pathways emerges due to weak intensity of longitudinal component: the more longitudinally polarized photons are involved, the weaker is the pathway with respect to the dominant ones that include at most two longitudinally polarized photons.

Chiral topological light opens the way to obtaining robust, topologically protected enantio-sensitive observables in randomly oriented chiral molecules. While here we focused on non-linear optical response other exciting applications include photoionization, transient absorption and enantio-manipulation using optical forces as well as the ambitious goal of obtaining quantized enantio-sensitive observables.
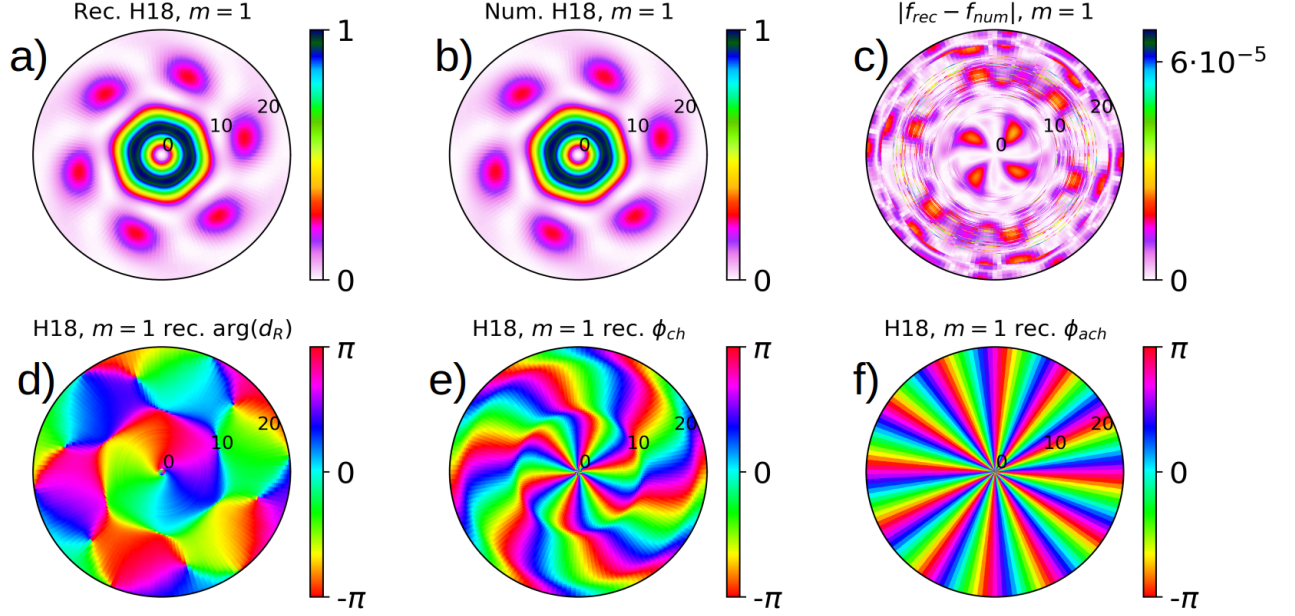
FIG. 4. Complete reconstruction of achiral and chiral components of the right-circularly polarized component (SAM $m = 1$) of H18 in Fenchone using a chiral vortex with $C = -6$ topological charge. **a)** Far-field profile obtained from the reconstruction algorithm. **b)** Far-field profile obtained from the SFA simulations. **c)** Normalized difference between the reconstructed and SFA profiles. **d)** Phase of the far-field dipole moment obtained from the reconstruction algorithm. **e)** Phase of the chiral component obtained from the reconstruction algorithm. **f)** Relative phase between the achiral components obtained from the reconstruction algorithm.

METHODS

A. Chiral correlation function

We report here the analytical expression for the chiral correlation function $h^{(5)}(-2\omega, -\omega, \omega, \omega, \omega) = \mathbf{E}^*(2\omega) \cdot [\mathbf{E}^*(\omega) \times \mathbf{E}(\omega)] (\mathbf{E}(\omega) \cdot \mathbf{E}(\omega))$ for the general case of two OAM-carrying beams with frequencies ω and 2ω, SAM m_ω and $m_{2\omega}$ and OAM ℓ_ω and $\ell_{2\omega}$.

$$h^{(5)}(\rho,\theta) = -\frac{\mathcal{E}_{2\omega}\mathcal{E}_\omega^4}{\sqrt{2}2k_\omega^2}e^{-5\frac{\rho^2}{W_0^2}}\left(\frac{\sqrt{2}}{W_0}\right)^{4|\ell_\omega|+|\ell_{2\omega}|}$$

$$\rho^{4|\ell_\omega|+|\ell_{2\omega}|-3}\left(|\ell_\omega|-m_\omega\ell_\omega-\frac{2\rho^2}{W_0^2}\right)^2$$

$$\left\{\frac{|\ell_\omega|-m_\omega|\ell_\omega|-2\frac{\rho^2}{W_0^2}}{2k_\omega}\left[e^{im_\omega\theta}(m_\omega-m_{2\omega})-\right.\right.$$

$$e^{-im_\omega\theta}(m_\omega+m_{2\omega})\big]$$

$$+\frac{m_{2\omega}}{k_{2\omega}}(|\ell_{2\omega}|-m_{2\omega}\ell_{2\omega}-\frac{2\rho^2}{W_0^2})e^{-im_{2\omega}\theta}\bigg\}$$

$$e^{i(2\phi_\omega-\phi_{2\omega})}e^{i(2\ell_\omega+2m_\omega-\ell_{2\omega})\theta} \tag{7}$$

It is easy to verify that both in the counter-rotating $m_\omega = -m_{2\omega}$ and co-rotating case $m_\omega = m_{2\omega}$ the azimuthal dependence of the chiral correlation function is given by $C\theta$, where $C = 2(\ell_\omega + m_\omega) - (\ell_{2\omega} + m_{2\omega})$.

B. DFT-based SFA simulations in Fenchone

The dipole moment for the given enantiomer and harmonic order is computed as

$$\mathbf{D}(N\omega) = \int d\Omega \int d\beta \, \mathbf{D}_{\Omega\beta}(N\omega)$$

where

$$\mathbf{D}_{\Omega\beta}(N\omega) = e^{iN\Omega t_r'} a_{rec} \, \mathbf{d}(U_{\Omega\beta}Re[\mathbf{k}(t_r')]) a_{prop} \quad (8)$$
$$e^{-iS(\mathbf{p}_s,t_i,t_r)} \, a_{ion} \, \tilde{\Psi}_{\Omega\beta}(U_{\Omega\beta}Re[\mathbf{k}(t_i')]) \quad (9)$$

where $\mathbf{d}(k)$ is the recombination matrix element in the laboratory frame. Here $U_{\Omega\beta}$ is the rotation matrix that transform the laboratory to the molecular frame. The integral over the solid angle $d\Omega = d\alpha d\beta \sin(\beta)$ is performed by Lebedev quadrature, while the integral over the β angle is done by trapezoid method. In order to find the rotation matrix, we first assume that the x-axis of the molecular frame x_M points toward the given Lebedev point and then rotate by an angle β around the x-axis. For all simulations we used a 17th order Lebedev quadrature (for a total of 110 points) and 40 β angles evenly distributed on the $[0, 2\pi]$ interval.

In the dipole expression, $\mathbf{p}$, $t_i = t_i' + it_i''$, $t_r = t_r' + it_r''$ are the complex saddle momenta and complex times of ionization and recombination. $S(\mathbf{p}, t_i, t_r) = 2^{-1}\int_{t_i}^{t_r} dt' \, [\mathbf{p}+\mathbf{A}(t')]^2 + I_p(t_r - t_i)$ is the action from the (complex) times of ionization and recombination. The terms associated with the saddle point method on $(t_i, t_r, \mathbf{p})$ are given by

$$a(\mathbf{p}, t_i, t_r) = a_{ion}a_{prop}a_{rec}$$

$$a_{ion} = \sqrt{\frac{2\pi}{\partial_{t_i}^2 S}}$$

$$a_{rec} = \sqrt{\frac{2\pi}{\partial_{t_r}^2 S}}$$

$$a_{prop} = \left(\frac{2\pi}{i(t_r - t_i)}\right)^{3/2}$$

where the second derivatives of the action are given explicitly by

$$\partial_{t_i}^2 S = -\mathbf{E}(t_i) \cdot \mathbf{k}(t_i)$$

$$\partial_{t_i}^2 S = \mathbf{E}(t_r) \cdot \mathbf{k}(t_r)$$

where $\mathbf{E}(t)$ is the electric field. and all expressions for the prefactor are calculated at the complex times.

The transition matrix elements of the right and left-handed molecules are related by

$$\mathbf{D}_R(k) = -\mathbf{D}_L(-k) \quad (10)$$

while for the Dyson orbital we use the relation

$$\Psi_D^R(\mathbf{k}) = \Psi_D^L(-\mathbf{k}) \quad (11)$$

The matrix elements for Fenchone are calculated using DFT methods described in [15, 18].

C. Noise simulations

In order to include the effect of noise on HHG driven by chiral vortex light, we take the following approach. For a given electric field strength E_0 (which we assume to be the same for both fields) the Laguerre-Gaussian beam is given in the near-field by $\mathbf{E}(\mathbf{r}) = E_0\mathbf{LG}_{l,p}(\mathbf{r})$, where $\mathbf{LG}_{l,p} = LG_{l,p}(\mathbf{r})\mathbf{e}_L(\mathbf{r})$. Here $LG_{l,p}$ is a Laguerre-Gaussian mode and $\mathbf{e}_L$ is the polarization vector of the field. The corresponding laser intensity is $I_0 = |E_0|^2$. We then pick a value for the laser intensity from a normal distribution of noise centered at I_0 with width γ. We call this electric field intensity I_1. Then, for each point $\mathbf{r}$ in the focus, we introduce intensity fluctuations such that at a given position the electric field strength is given by

$$\mathcal{I}(\mathbf{r}) = I_1 \, LG_{l,p}(\mathbf{r})(1 + \delta_I(\mathbf{r})) \quad (12)$$

where $\delta_I(\mathbf{r}) = C\lambda(\mathbf{r})$. $\lambda(\mathbf{r})$ is chosen from a Gaussian distribution centered at zero with width 1 and $C = 0.1$ is a constant. There is therefore 68.2% probability that the fluctuation will be below 0.1% of the signal at the given point. We produce 50 electric fields using this approach, choosing a central intensity of $I_0 = 5 \cdot 10^{14}$ W/cm^2 with width $\gamma = 3.51 \cdot 10^{13}$ W/cm^2.

For the results show in Fig. 3f, we scan the enantiomeric excesses ee between -100% and 100% with steps of $\Delta ee = 0.05\%$, and pick randomly one of the 50 shots for each single ee value. After performing the Fourier analysis for each ee value, we obtain the phase of the Fourier component f_6 by performing a moving average with window size of $\Delta ee = 5\%$.
For the phase reconstruction algorithm, we apply it to a far-field image obtained by averaging the 50 noisy shots $S_{avg} = \sum_{i=1}^{50} S_i$. The results of the reconstruction algorithm is shown in Figs. 4,5,6 of the Supplementary Information.

I. MULTIPHOTON PICTURE

The alternative multiphoton picture of enantiosensitive HHG driven by chiral vortices can be understood by analyzing the contributing chiral and achiral multiphoton pathways. To do so, we classify the multiphoton pathways by indicating with a subscript the SAM of the photon, so that e.g. $(N)\omega_+$ indicate the absorption of N ω photons with SAM $m = 1$ and $(-1)\omega_z$ indicates the emission of one ω photon with SAM $m = 0$.

In the specific case of bicircular counter-rotating fields, if the field has no longitudinal component along its direction of propagation (i.e. if we consider an achiral field in the dipole approximation), conservation of SAM results in an harmonic spectrum with doublets at $3N+1$ and $3N+2$ harmonic frequencies, where the $3N+1$ harmonics ($3N+2$) co-rotate with the ω (2ω) field [19]. $3N$ harmonic orders are forbidden in achiral media, since their generation requires absorption of an equal number of photons from both drivers. In chiral media, the $3N$ harmonic orders can instead be generated due to the broken parity of the medium, but are polarized along the direction of propagation of the fields (the z-axis in our case), and thus are not detectable in the far-field. We label this pathway as

$$C_z = [(N)\omega_+, (N)2\omega_-].\qquad(13)$$

Focusing on the specific case of 3N harmonic orders, if the field is chiral (i.e. if it posses a longitudinal component along the propagation direction) in the case of achiral media the following multiphoton pathways can now lead to symmetry-allowed HHG:

$$AC_+ = [(N-2)\cdot\omega_+, (2)\omega_z, (N-1)\cdot 2\omega_-]\qquad(14)$$
$$AC_- = [(N-1)\cdot\omega_+, (-1)\omega_z, (N)\cdot 2\omega_-, (1)2\omega_z]\qquad(15)$$

corresponding respectively to the emission of a photon with SAM $m = 1$ and $m = -1$. We label these pathways as achiral pathways (i.e. AC_m, with m the SAM of the harmonic photon), since they occur already in achiral media driven by a chiral field as they require the absorption and emission of an odd number of photons. If the medium is chiral, two new pathways including absorption of an equal number of ω and 2ω photons open, i.e.

$$C_+ = [(N)\cdot\omega_+, (N-1)\cdot 2\omega_-, (1)2\omega_z]\qquad(16)$$
$$C_- = [(N-1)\cdot\omega_+, (1)\omega_z, (N)\cdot 2\omega_-]\qquad(17)$$

corresponding again respectively to the emission of a photon with SAM $m = 1$ and $m = -1$. We label these pathways as chiral pathways (C_m) since they can occur only in chiral media. Finding the corresponding OAM of all pathways indicated above is straightforward, once we remember that the longitudinal components of the fields carry OAMs of $\ell_{\omega_z} = \ell_{\omega_+} + m_\omega$ and $\ell_{2\omega_z} = \ell_{2\omega_-} + m_{2\omega}$. Obviously, other chiral and achiral pathways including the absorption of a larger number of z-polarized photons from either drivers are also in principle accessible: yet, since the longitudinal component is relatively weak, we restrict ourselves here to the photon pathways that include the absorption or emission of the fewest number of z-polarized photons. Fig. 1a of the Supplementary Information) shows schematically the multiphoton pathways C_z, AC_m and C_m for the case of a 3N harmonic order.

The results from the SFA simulations confirm the considerations above; in Fig. 1b of the Supplementary Information) we show the near-field OAM distributions for H18 in (+)Fenchone driven by a field with $\ell_\omega = -\ell_{2\omega} = 1$ and $m_\omega = -m_{2\omega} = 1$. For comparison, we also report the OAM content for an artificial atom with ionization potential equal to Fenchone driven by the same chiral field and the OAM content in Fenchone for an achiral field with same OAM of the driving beams, obtained by manually setting the longitudinal component of the field to zero.

When the field is achiral, H18 in an atom is absent, while in the case of Fenchone we observe a $\ell = 0$ component polarized along the z-axis: this corresponds to the pathway C_z denoted above. When the field is chiral, circularly polarized components with $\ell = \pm 5$ are observed for both the atom and the molecule: these are the achiral pathways AC_+ and AC_- denoted above. Finally, the chiral pathways C_+ and C_- correspond to the OAMs $\ell = \pm 1$ and are only seen in a chiral molecule, since they require the absorption of an even number of photons. Note that in the far-field only the SAM $m = \pm 1$ components are going to be observed, since $m = 0$ polarization (corresponding to the C_z pathway in black in Fig. 1 of the Supplementary Information) will propagate in a direction orthogonal with respect to the propagation axis of the beams.

The different OAM content of an atom and chiral molecule driven by a chiral bicircular field is directly reflect in the far-field profile of H18, shown in Fig. 1c of the Supplementary Information). In an atom (left figure of Fig. 1 of the Supplementary Information), where for a given SAM there is only one contributing OAM, the far-field profile of H18 is a ring where the intensity is mostly constant, while in Fenchone we observe an azimuthal interference pattern with periodicity determined by the topological charge C, corresponding in modulus to the net difference between the OAMs of chiral and achiral pathways. The enantio-sensitive rotation of the spatial profile can be understood from the perspective of the multiphoton pathways by accounting a shift by π of the phase of the chiral pathways $C_\pm$ when changing the molecular enantiomer. The enantio-sensitive rotation of the spatial profile of the high-harmonics in the far-field allows one also to use HHG driven by chiral vortices as a highly-sensitive method to infer the enantiomeric excess in a mixture of right and left molecular enantiomers.

[1] Binghai Yan and Shou-Cheng Zhang. Topological materials. *Rep. Prog. Phys.*, 75(096501), 2012.

[2] Sanju Gupta and Avadh Saxena. A topological twist on materials science. *MRS Bulletin*, 39(3):265–279, 2014.

[3] Á. Jiménez-Galán, R. E. F. Silva, O. Smirnova, and M. Ivanov. Lightwave control of topological properties in 2d materials for sub-cycle and non-resonant valley manipulation. *Nat. Photon.*, 14:728–732, 2020.

[4] R. E. F. Silva, Á. Jiménez-Galán, B. Amorim, O. Smirnova, and M. Ivanov. *Nat. Photon.*, 13:849–854, 2019.

[5] M. Z. Hasan and C. L. Kane. Colloquium: Topological insulators. *Rev. Mod. Phys.*, 82:3045–3067, Nov 2010.

[6] Alexander B. Khanikaev, S. Hossein Mousavi, Wang-Kong Tdse, Mehdi Kargarian, Allan H. MacDonald, and Gennady Shvets. Photonic topological insulators. *Nat. Mater.*, 12:233–239, 2013.

[7] Andres F. Ordonez and Olga Smirnova. A geometric approach to decoding molecular structure and dynamics from photoionization of isotropic samples. *Phys. Chem. Chem. Phys.*, 24:13605–13615, 2022.

[8] Andres F. Ordonez, David Ayuso, Piero Decleva, and Olga Smirnova. Geometric fields and new enantio-sensitive observables in photoionization of chiral molecules. *arXiv*, (arXiv:2106.14264), 2021.

[9] Kai Schwennicke and Joel Yuen-Zhou. Enantioselective topological frequency conversion. *The Journal of Physical Chemistry Letters*, 13(10):2434–2441, 2022. PMID: 35259295.

[10] Kai Schwennicke and Joel Yuen-Zhou. Optical activity from the exciton aharonov–bohm effect: A floquet engineering approach. *The Journal of Physical Chemistry C*, 124(7):4206–4214, 2020.

[11] Y. Shen, X. Wang, Z. Xie, C. Min, X. Fu, Q. Liu, M. Gong, and X. Yuan. Optical vortices 30 years on: Oam manipulation from topological charge to multiple singularities. *Light: Science & Applications*, 8(90), 2019.

[12] J. R. Rouxel and et al. Hard x-ray helica dichroism of disordered molecular media. *Nat. Photon.*, 16:570–574, 2022.

[13] J. R. Rouxel and S. Mukamel. Molecular chirality and its monitoring by ultrafast x-ray pulses. *Chem. Rev.*, 122(22):16802–16838, 2022.

[14] D. Ayuso and et al. Synthetic chiral light for efficient control of chiral light–matter interaction. *Nat. Phot.*, 13:866–871, 2019.

[15] David Ayuso, Andres F Ordonez, Piero Decleva, Misha Ivanov, and Olga Smirnova. Enantio-sensitive unidirectional light bending. *Nature Communications*, 12(1):1–9, 2021.

[16] Margarita Khokhlova, Emilio Pisanty, Serguei Patchkovskii, Olga Smirnova, and Misha Ivanov. Enantiosensitive steering of free-induction decay. *arXiv preprint arXiv:2109.15302*, 2021.

[17] Ofer Neufeld, David Ayuso, Piero Decleva, Misha Y. Ivanov, Olga Smirnova, and Oren Cohen. Ultrasensitive chiral spectroscopy by dynamical symmetry breaking in high harmonic generation. *Phys. Rev. X*, 9:031002, Jul 2019.

[18] D Toffoli, M Stener, G Fronzoni, and P Decleva. Convergence of the multicenter b-spline dft approach for the continuum. *Chemical Physics*, 276(1):25–43, 2002.

[19] Daniel D Hickstein, Franklin J Dollar, Patrik Grychtol, Jennifer L Ellis, Ronny Knut, Carlos Hernández-García, Dmitriy Zusin, Christian Gentry, Justin M Shaw, Tingting Fan, et al. Non-collinear generation of angularly isolated circularly polarized high harmonics. *Nature Photonics*, 9(11):743–750, 2015.